Dalton Transactions

ROYAL SOCIETY OF CHEMISTRY

PAPER

View Article Online
View Journal | View Issue

Cite this: *Dalton Trans.*, 2024, **53**, 7971

From field-induced to zero-field SMMs associated with open/closed structures of bis(ZnDy) tetranuclear complexes: a combined magnetic, theoretical and optical study†

Andoni Zabala-Lekuona, *[a] Xabier Lopez de Pariza, [b] Ismael F. Díaz-Ortega, [c,d] Javier Cepeda, [a] Hiroyuki Nojiri, [d] Nina P. Gritsan, [e] Alexey A. Dmitriev, [e] Alberto López-Ortega, [f,g,h] Antonio Rodríguez-Diéguez, [i] José M. Seco *[a] and Enrique Colacio *[i]

We have prepared a bis(compartmental) Mannich base ligand H_4L (1,4,8,11-tetraaza-1,4,8,11-tetrakis(2-hydroxy-3-methoxy-5-methylbenzyl)cyclotetradecane) specifically designed to obtain bis($TM^{II}Ln^{III}$) tetranuclear complexes (TM = transition metal). In this regard, we have succeeded in obtaining three new complexes of the formula $[Zn_2(\mu\text{-}L)(\mu\text{-}OAc)Dy_2(NO_3)_2]\cdot[Zn_2(\mu\text{-}L)(\mu\text{-}OAc)Dy_2(NO_3)(OAc)]\cdot 4CHCl_3\cdot 2MeOH$ (**1**) and $[TM_2(\mu\text{-}H_2L)_2(\mu\text{-succinate})Ln_2(NO_3)_2]\ (NO_3)_2\cdot 2H_2O\cdot 6MeOH$ (TM^{II} = Zn, Ln^{III} = Dy (**2**); TM^{II} = Co, Ln^{III} = Dy (**3**)). Compound **1** contains two different bis(ZnDy) tetranuclear molecules that cocrystallize in the structure, in which acetato bridging ligands connect the Zn^{II} and Dy^{III} ions within each ZnDy subunit. This compound does not exhibit slow magnetic relaxation at zero field, but it is activated in the presence of an applied dc magnetic field and/or by Dy/Y magnetic dilution, showing two relaxation processes corresponding to each of the two different bis(ZnDy) units found in the structure. As revealed by the theoretical calculations, magnetic relaxation in **1** is single-ion in origin and takes place through the first excited state of each Dy^{III} ion. When using the succinato dicarboxylate bridging ligand instead of acetate, compounds **2** and **3** were serendipitously formed, which have a closed structure with the succinate anion bridging two ZnDy subunits belonging to two different ligands. It should be noted that only compound **2** exhibits slow relaxation of magnetization in the absence of an external magnetic field. According to experimental and theoretical data, **2** relaxes through the second excited Kramers doublet (U_{eff} = 342 K). In contrast, **3** displays field-induced SMM behaviour (U_{eff} = 203 K). However, the Co/Zn diluted version of this compound $\mathbf{3_{Zn}}$ shows slow relaxation at zero field (U_{eff} = 347 K). *Ab initio* theoretical calculations clearly show that the weak ferromagnetic coupling between Co^{II} and Dy^{III} ions is at the origin of the lack of slow relaxation of this compound at zero field. Compound **2** and its diluted analogues $\mathbf{2_Y}$ and $\mathbf{3_{Zn}}$ show hysteresis loops at very low temperature, thus confirming their SMM behaviour. Finally, compounds **1** and **2** show Dy^{III} based emission even at room temperature that, in the case of **2**, allows us to extract the splitting of the ground $^6H_{15/2}$ term, which matches reasonably well with theoretical calculations.

Received 17th January 2024,
Accepted 11th April 2024

DOI: 10.1039/d4dt00148f

rsc.li/dalton

[a]*Departamento de Química Aplicada, Facultad de Química, Universidad del País Vasco (UPV/EHU), 20018 Donostia-San Sebastián, Spain. E-mail: andoni.zabala@ehu.eus, josemanuel.seco@ehu.eus*

[b]*POLYMAT and Department of Polymers and Advanced Materials: Physics, Chemistry and Technology, Faculty of Chemistry, University of the Basque Country UPV/EHU, Paseo Manuel de Lardizabal 3, Donostia-San Sebastián 20018, Spain*

[c]*Departamento de Química y Física-CIESOL, Universidad de Almería, Ctra. Sacramento s/n, 04120 Almería, Spain*

[d]*Institute for Materials Research, Tohoku University, Katahira, Sendai, 980-8577, Japan*

[e]*Institute of Chemical Kinetics and Combustion, Siberian Branch, Russian Academy of Sciences, 630090 Novosibirsk, Russia*

[f]*Departamento de Ciencias, Universidad Pública de Navarra, E-31006 Pamplona, Spain*

[g]*Institute for Advanced Materials and Mathematics (INAMAT2), Universidad Pública de Navarra, E-31006 Pamplona, Spain*

[h]*CIC nanoGUNE BRTA, Tolosa Hiribidea 76, Donostia-San Sebastian, 20018, Spain*

[i]*Departamento de Química Inorgánica, Facultad de Ciencias, Universidad de Granada, 18071 Granada, Spain. E-mail: ecolacio@ugr.es*

† Electronic supplementary information (ESI) available. CCDC 2226682–2226685. For ESI and crystallographic data in CIF or other electronic format see DOI: https://doi.org/10.1039/d4dt00148f

Introduction

Single-molecule magnets (SMMs) are open-shell coordination compounds displaying slow relaxation of magnetization and, as a result, magnetic hysteresis and magnetic memory below the so-called blocking temperature (T_B).[1] These properties make SMMs potential candidates for magnetic data storage[2] and molecular spintronic[3] devices. The SMM behavior mainly depends on the magnetic anisotropy, which arises from the combined action of spin–orbit coupling (SOC) and ligand field effects. Therefore, it is not surprising that the best SMM properties have been observed for metal complexes containing very anisotropic lanthanide ions, particularly Dy^{III}. In fact, dysprosocenium analogues have been shown to be very efficient as SMMs with a U_{eff} (effective energy barrier for magnetization reversal) of up to 1540 cm^{-1} and T_B values surpassing the temperature limit of liquid nitrogen.[4] Even though many other factors should be considered, a fundamental one to observe SMM behaviour is the easy-axis anisotropy of the Dy^{III} ion. To achieve this requirement, the Dy^{III} ion should have as strong an axial field and as weak an equatorial ligand field as possible.[5] It is worth noting that T_B and U_{eff} are not always strictly linked, since under-barrier relaxation pathways may co-exist shortcutting the U_{eff} and diminishing the functional T_B value. Indeed, a wide variety of systems have recently been reported with large U_{eff} values, but with widely varying T_Bs[6–9] that are typically smaller than those expected based on U_{eff} values.

Inspired by these guidelines, we and others have prepared a series of aminophenol Mannich and Schiff based compartmental ligands that can simultaneously host both 3d and 4f ions in separate coordination pockets.[10–12] In such compounds, the largest negative charge, and consequently the largest ligand field, is provided by phenoxido groups, while the remaining neutral heteroatoms provide weaker ligand fields. Under these conditions, the magnetic anisotropy of the Dy^{III} ion mainly depends on the location of the phenoxido groups in the Dy^{III} coordination sphere. For instance, in trinuclear ZnDyZn complexes with two pairs of phenoxido groups placed at opposite positions of the Dy^{III} ion, the crystal field favours the easy-axis magnetic anisotropy, which usually leads to an improvement of the SMM properties. Moreover, the inclusion of diamagnetic Zn^{II} can also be an adjuvant factor to increase the easy-axis magnetic anisotropy of the Dy^{III} ion in this type of 3d–4f complex.[13] Additionally, it needs to be pointed out that when both (3d and 4f) paramagnetic ions are combined in a system, in some cases magnetic interactions suppress quantum tunnelling of magnetization (QTM). This fact could also favour the SMM behaviour at zero field, as observed in some strongly coupled CrDy or NiDy based compounds.[14,15] However, it should be noted that the strategy of combining two exchanged anisotropic metal ions into a compound does not ensure SMM behaviour even in the presence of an applied magnetic field.[16,17] Thus, in order to better understand the magnetic interactions between 3d and 4f ions and, most importantly, their effect on the SMM behaviour, it would be very useful to prepare relatively simple 3d–4f systems. In addition, lanthanides can emit light in both the visible and NIR regions.[18,19] Thus, multifunctional systems with magnetic and luminescence properties can be obtained. Besides, the emission bands are directly related to the electronic structure of the lanthanide ion, and therefore extremely valuable information could be obtained from the emission spectra.

In view of the foregoing, it becomes clear that the use of compartmental ligands to prepare relatively simple 3d–4f systems is still of paramount interest. In this regard, Comba *et al.*[17] are pioneers in preparing potential compartmental ligands by incorporating aminophenol groups as substituents at the nitrogen atoms of triaza- and tetraaza-macrocycles. These ligands allow the preparation of linear 3d–4f–3d trinuclear and 3d–4f dinuclear complexes, respectively.[17,20] In the latter case, no tetranuclear complexes were formed, since two of the aminophenol groups linked to the 1,4,7,10-cyclododecane macrocycle in alternating positions do not coordinate the metal ions. In this regard, and in order to obtain tetranuclear bis(ZnDy) compounds, we have designed and synthesized a novel Mannich ligand, 1,4,8,11-tetraaza-1,4,8,11-tetrakis(2-hydroxy-3-methoxy-5-methylbenzyl) cyclotetradecane, H_4L (Scheme 1). This ligand has four (two and two) individual pockets ideal for bis(3d–4f) systems, where all aminophenoxido groups would bridge 3d and 4f metal ions. These bis(3d–4f) systems can be connected by different linkers to give very interesting systems not only from a structural, but also from a magnetic point of view.

Herein, we report the X-ray single-crystal structures, dc and ac magnetic properties, theoretical *ab initio* calculations and photoluminescence properties of the following bis(3d–4f) complexes of the formula $[Zn_2(\mu\text{-}L)(\mu\text{-}OAc)Dy_2(NO_3)_2]\cdot[Zn_2(\mu\text{-}L)(\mu\text{-}OAc)Dy_2(NO_3)(OAc)]\cdot 4CHCl_3\cdot 2MeOH$ (**1**) and $[TM_2(\mu\text{-}H_2L)_2(\mu\text{-}succinate)Ln_2(NO_3)_2](NO_3)_2\cdot 2H_2O\cdot 6MeOH$ (TM^{II} = Zn, Ln^{III} = Dy (**2**); TM^{II} = Co, Ln^{III} = Dy (**3**)). The aim of this work is fourfold: (i) to confirm the formation of bis(ZnDy) tetranuclear complexes and to analyse how the nature of the carboxylate ancillary ligand (mono- or dicarboxylate) affects the final tetranuclear structure; (ii) to determine whether complexes **1** and **2** exhibit SMM behaviour and, if so, to perform theoretical ana-

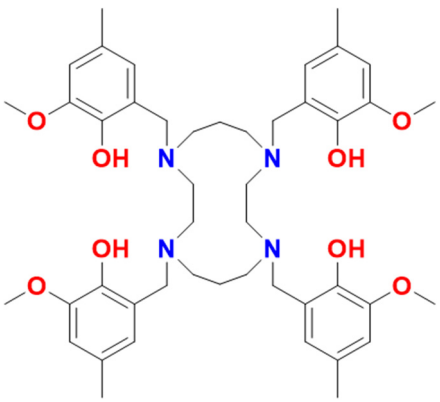

Scheme 1 Structure of ligand H_4L.

lysis of their electronic structure to support their magnetization relaxation mechanisms; (iii) to perform experimental and theoretical studies on compound **3**, as well as on its dilute counterparts $\mathbf{2_Y}$, $\mathbf{3_{Zn}}$ and $\mathbf{3_Y}$, which are isostructural versions of **2**, to elucidate the origin of the influence of the Co–Dy magnetic coupling on the SMM properties of **2**; and (iv) to study the luminescence properties of **1** and **2** and to correlate the structure of their experimental emission spectra with the theoretically calculated electronic structure.

Results and discussion

Synthetic procedures and details of the experimental and theoretical methodologies used to study the reported complexes are described in the ESI.†

The compartmental ligand H_4L (Scheme 1) possesses two double pockets. Each pocket consists of an inner N_2O_2 site suitable for transition metal ions and another outer O_4 site more suitable for harder oxophilic metal ions, such as lanthanides. Therefore, each ligand can give rise to two dinuclear systems in one, *i.e.* a bis(ZnDy) system, in which the macrocycle backbone links the ZnDy subunits. In good agreement with this, the reaction of H_4L with $Zn(OAc)_2{\cdot}2H_2O$, $Dy(NO_3)_3{\cdot}5H_2O$ and Et_3N in a $CHCl_3$/MeOH solvent mixture produced the tetranuclear bis(ZnDy) complex (**1**). In **1**, the Zn^{II} and Dy^{III} ions within each dinuclear subunit are bridged by an acetate group. Each ZnDy subunit is very similar in the coordination environment of metal ions to the acetate-bridged dinuclear compound we reported previously.[10] In the synthesis of compounds **2–3**, H_4L reacted with the corresponding TM $(NO_3)_2{\cdot}xH_2O$ and $Ln(NO_3)_3{\cdot}xH_2O$ in methanol in the first step, and with succinic acid and Et_3N in the second step. The final complexes **2–3** exhibit a closed bis(TMLn) tetranuclear structure in which two dinuclear TMLn units are bridged by two aminophenolate groups belonging to neighbouring ligands and a succinate linker.

Crystal structures

The compartmental ligand H_4L crystallizes in the triclinic $P\bar{1}$ space group. The asymmetric unit consists of half of the ligand, where the phenol groups are stabilized by intramolecular hydrogen bonds towards amines (crystallographic data are given in Table S3,† and the structure is shown in Fig. S1†).

Compound **1** crystallizes in the monoclinic $P2/c$ space group (Table S3† for crystallographic data). The asymmetric unit contains two different half molecules and three crystallization solvent molecules (two chloroform and one methanol molecules). As mentioned above, two slightly different structures co-crystallize within the crystal structure, which will be referred to as **1A** and **1B** hereinafter (Fig. 1). In both cases, the fully deprotonated L^{4-} ligand encapsulates two pairs of $Zn^{II}Dy^{III}$ systems, which are triply bridged by two phenoxido groups of the main ligand and one *syn–syn* acetate group. In both **1A** and **1B**, the transition metal possesses the same

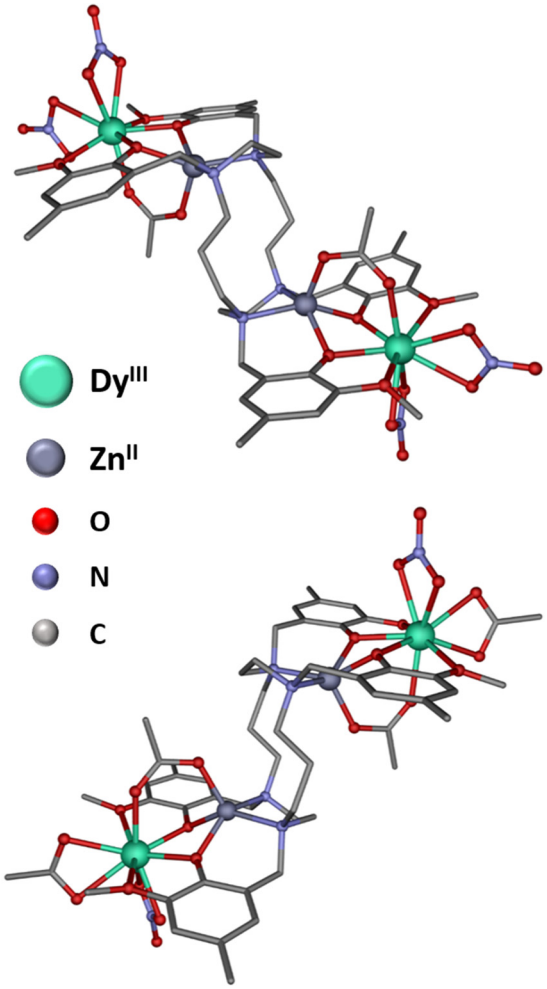

Fig. 1 Perspective view of the molecular structure of **1** (**1A** top panel and **1B** bottom panel). Hydrogen atoms are omitted for clarity.

ZnN_2O_3 square pyramidal coordination environment according to SHAPE[21] calculations (Table S6†). The shortest bond lengths correspond to Zn–O (1.969(2)–2.064(2) Å), while the Zn–N distances are somewhat longer (2.140(3)–2.221(3) Å).

The difference between **1A** and **1B** (besides bond distances and angles, Table S4†) lies in the coordination environment of the Dy^{III} ions. They both exhibit DyO_9 coordination spheres, and seven of the nine oxygen atoms belong to the same groups, namely, two phenoxido and two methoxy belong to L^{4-}, two oxygen atoms come from the bidentate nitrate and one oxygen belongs to the bridging acetate. The last two oxygen atoms, however, belong to an additional bidentate nitrate in **1A** and another additional chelating acetate in **1B**. In terms of bond lengths, Dy–O bonds fall into four different categories: the shortest $Dy–O_{phenoxido}$ bonds (in the range of 2.262(2)–2.285(2) Å), intermediate $Dy–O_{\mu\text{-acetate}}$ (2.329(3) Å and 2.346(3) Å), longer $Dy–O_{nitrate}$ (between 2.441(3) and 2.500(3) Å) and the longest $Dy–O_{methoxy}$ (in the range of 2.515(2)–2.572(2) Å). For the chelating acetate, the $Dy–O_{acetate}$ bond lengths are longer than those for bridging acetate, but shorter than those

of Dy–$O_{nitrate}$: 2.407(3) Å and 2.441(3) Å. Although the differences between **1A** and **1B** are small, they seem to have a significant effect on the dynamic magnetic properties related to them (*vide infra*). SHAPE analysis shows that the coordination polyhedra in both cases are far from ideal symmetry, but in both cases, they best fit a capped square antiprism (Table S7†). Finally, the shortest intermolecular $Dy^{III}\cdots Dy^{III}$ distance is 8.3079(7) Å, while intramolecular distances are 12.3011(6) Å and 12.1047(6) Å for **1A** and **1B**, respectively.

Compounds **2** and **3** are isostructural and crystallize in the orthorhombic *Pba*2 space group (for crystallographic data, see Table S3†). In view of this, only compound **2** will be described hereinafter as an example. The X-ray crystal structure of **2** consists of the $[Zn_2(\mu\text{-}H_2L)_2(\mu\text{-succinate})Dy_2(NO_3)_2]^{2+}$ cation, two NO_3^- anions, six methanol and two water crystallization molecules (Fig. 2).

Only one of the two double pockets in each ligand acts as predicted, encapsulating a dinuclear $Zn^{II}Dy^{III}$ entity. As for the other pocket, only one aminophenolate group coordinates to the Dy^{III} ion (located in the pocket of the other H_2L^{2-} ligand) in a bidentate form *via* the oxygen atoms of the phenoxido and methoxy groups, while the other aminophenol group remains uncoordinated with the phenol group in the protonated state. Hence, three of the four phenol groups are deprotonated, acting as $Zn^{II}Dy^{III}$ bridging phenoxido groups (O1 and O3 from the pocket) or as monocoordinating non-bridging phenoxido group (O7). Nonetheless, the ligands exhibit the H_2L^{2-} mode, since part of them have a zwitterionic form. More specifically, the protons from O7 migrate to the nearest amine N4, forming one asymmetric centre in each ligand, which is stabilized by a hydrogen bond between N4H⋯O7. Taking into account that the asymmetric unit contains only half of the molecule, both new centres in the molecule have the same configuration (*R*, *R*′ or *S*, *S*′). However, bearing in mind that there is no chiral directing agent to force the structure to be one enantiomer or the other, they both co-crystallize in the crystal structure (Fig. S2†). The role of the succinate ligand is essential in this structure because it acts as a double bridging group. On the one hand, it forms a bridge between Zn^{II} and Dy^{III} ions in the same way as in **1**, and, on the other, it connects two dinuclear entities located in the pocket of each ligand.

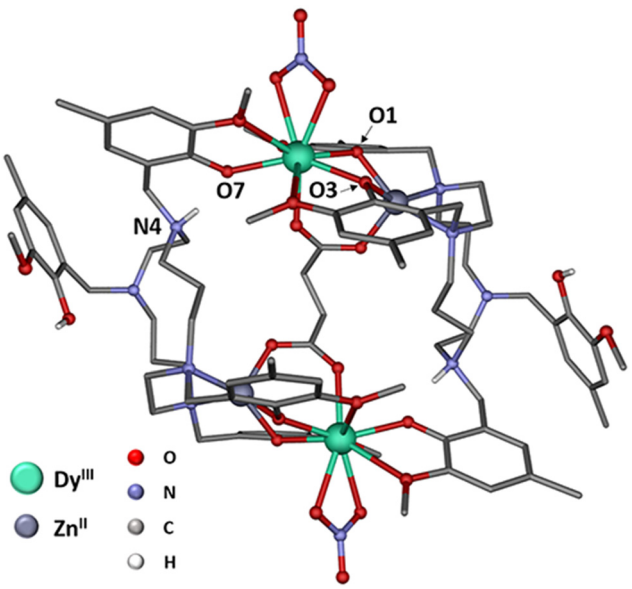

Fig. 2 Perspective view of the molecular structure of compound **2**. Hydrogen atoms (except the phenolic and zwitterionic ones) and the counterions are omitted for clarity.

In **2**, the ZnN_2O_3 coordination sphere is very similar to that in **1**. However, although the DyO_9 coordination environment is formed by the same seven out of nine oxygen atoms belonging to the same groups as in **1** (two phenoxido, two methoxy, two nitrate and one succinate oxygen atoms), the additional chelate nitrate (or acetate in **1B**) is replaced by a chelate formed by the oxygen atoms of the phenoxido and methoxy groups of the neighbouring ligand, resulting in a distorted muffin geometry (Table S7†). Therefore, the ZnDy subunits are connected by two aminophenolate groups belonging to neighbouring ligands and by a bis(chelate) succinate connector, forming a closed structure. Dy–$O_{phenoxido}$ bond lengths are the shortest ones in the range of 2.227(4)–2.313(4) Å, the Dy–$O_{carboxylate}$ is slightly longer at 2.320(4) Å and the rest of Dy–O lengths are larger than 2.4 Å (Table S5†). Remarkably, among the wide variety of donor atoms in this system, the most negatively charged phenoxido groups somehow provide the system with an appropriate crystal field leading to an axial ground state, which favours the SMM behaviour. Indeed, open angles with values of 137.32(16)° and 143.73(15)°are found between O1–Dy1–O7 and O3–Dy1–O7, respectively. As will be shown in the following sections, such a ligand field is important in explaining the dynamic magnetic properties of this system.

Within the molecule, the $Dy^{III}\cdots Dy^{III}$ and $Zn^{II}\cdots Zn^{II}$ distances are 8.6991(6) Å and 7.6269(9) Å, respectively, and the shortest intermolecular $Dy^{III}\cdots Dy^{III}$ and $Zn^{II}\cdots Zn^{II}$ distances are 10.8644(6) Å and 11.5391(9) Å, respectively. In compound **2**, the solvent molecules could not be properly refined. However, Fig. S3 and S4† show the supramolecular structure of **3** to clarify how these molecules are arranged in the 3D structure. It is worth mentioning that nitrate counterions as well as methanol and water molecules form a complex hydrogen-bonding pattern along the *b* axis (Fig. S3†), while the cationic $[Co_2(\mu\text{-}H_2L)_2(\mu\text{-succinate})Dy_2(NO_3)_2]^{2+}$ units are linked by hydrogen bonds between O5H⋯O3N. Thus, the cationic fragments grow to form a 2D framework in the *ab* plane (Fig. S4†).

Static magnetic properties

The temperature dependence of the $\chi_M T$ product (χ_M being the molar susceptibility) of polycrystalline samples of complexes **1**–**3** in the 2–300 K temperature range at an applied field of 0.1 T is given in Fig. 3. The room temperature $\chi_M T$ values for **1** and **2** of 57.90 and 28.26 $cm^3\ mol^{-1}\ K$, respectively, are in the expected ranges for four and two non-interacting Dy^{III} ions (14.17 $cm^3\ mol^{-1}\ K$; $^6H_{15/2}$, and $g = 4/3$). Compound **3**, containing additional anisotropic Co^{II} ions, has a value of 33.95 $cm^3\ mol^{-1}\ K$ at room temperature, which is greater than the

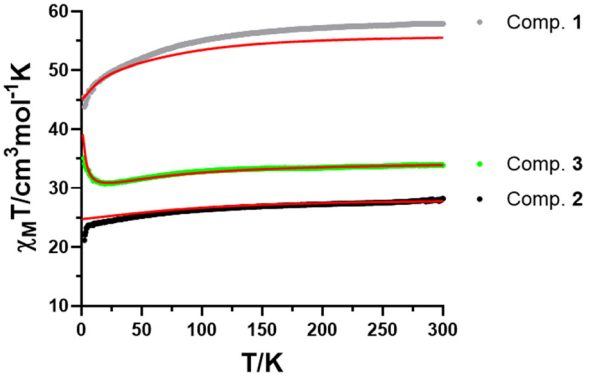

Fig. 3 Experimental temperature dependences of the $\chi_M T$ product under a field of 0.1 T for complexes **1–3** and the SINGLE_ANISO (**1** and **2**) and POLY_ANISO (**3**, J = 0.48 cm^{-1}) simulated data using the results of *ab initio* calculations (solid red lines).

expected value for two Co^{II} (with S = 3/2 and g = 2; 1.875 cm^3 mol^{-1} K) and two Dy^{III} ions of 32.09 cm^3 mol^{-1} K. This fact is mainly due to the unquenched orbital angular momentum of Co^{II} ions. Complexes containing a sole type of anisotropic ion (**1** and **2**) demonstrate the usual temperature dependence of the $\chi_M T$ product. Thus, $\chi_M T$ gradually decreases with decreasing temperature due to the depopulation of the M_J sublevels of the Dy^{III} ion arising from the splitting of multiplets by the ligand field. The final drastic drop for **2** could be indicative of magnetic blocking.[22] In contrast, for compound **3**, a gradual decrease in $\chi_M T$ is followed by a sharp increase below 25 K, reaching a value of 35.08 cm^3 mol^{-1} K at 2 K. This behaviour below 25 K clearly indicates the existence of a ferromagnetic coupling between Co^{II} and Dy^{III} ions *via* bis(phenoxido)succinate bridges. As can be seen in Fig. 3, $\chi_M T$ *vs.* T curves for **1–3** are very well reproduced by theoretical calculations (see below in the "Theoretical studies" section). For all compounds, there is both a lack of saturation (Fig. S5 and S6†), and some non-superimposable features in the reduced magnetization curves (Fig. S7 and S8†) in the 2–5 K temperature range, which suggests the occurrence of magnetic anisotropy.

Dynamic magnetic properties

At zero field, only compound **2** exhibits well-defined maxima in the $\chi''_M(T)$ plot below 28 K. Compounds **1** and **3** display non-zero signals, but without maxima (Fig. S9 and S10†). This may be due to the presence of a fast QTM process that prevents SMM behaviour. In order to suppress it, well known techniques have been used, such as the application of external dc fields and magnetic dilution in isostructural diamagnetic matrices.[23–25]

Frequency and temperature dependent ac susceptibility measurements were performed under an optimum dc field of 2.5 kOe for **1** (see field optimization data in Fig. S11 and S12†). To estimate the relaxation times of the two observed processes (FR, fast relaxation and SR, slow relaxation) the $\chi''_M(\nu)$ curves were fitted in the temperature range of 2.0–2.6 K and 7.0–13.0 K, respectively (Fig. S15 and S16†). The significant difference in operating temperatures for these processes allowed us to make this distinction. It is worth mentioning that for the FR process, only data above 1000 Hz were fitted to the generalized Debye model, since data below this frequency are significantly affected by the SR process.

The temperature dependence of the magnetization relaxation time in molecules exhibiting slow relaxation of the magnetization is commonly described by eqn (1):

$$\tau^{-1} = AH^4T + B_1/(1 + B_2H^2) + CT^n + \tau_0^{-1}\exp(-U_{\text{eff}}/k_BT) \quad (1)$$

where the first two terms correspond to the field dependent direct and QTM relaxation processes, respectively, whereas the third and fourth terms represent the field independent Raman and Orbach relaxation processes, respectively. Despite the high α values obtained from the Cole–Cole plots for **1** in both regimes (FR: 0.37 (2.0 K)–0.62 (2.6 K); SR: 0.52 (7.0 K)–0.49 (13.0 K)), which may be due to the mixing of the FR and SR processes, the temperature dependence of the relaxation times can be fitted to the Orbach process (Fig. 4). The best fit U_{eff} and τ_0 values are given in Table 1. Additional data analysis was accomplished using the CCFIT software.[26] This methodology gave results comparable to those obtained by separating the two temperature regimes (Fig. S19†).

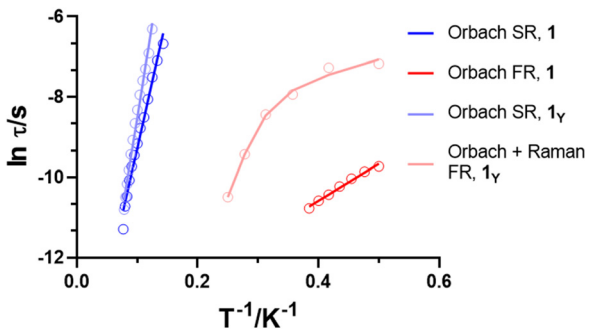

Fig. 4 Arrhenius plot for relaxation times for **1** and $\mathbf{1_Y}$ under 2.5 kOe applied field.

Table 1 U_{eff}, τ_0, C, n, and τ_{QTM} parameters generated from the fit of the relaxation time–temperature dependence for **1**, $\mathbf{1_Y}$, **2**, $\mathbf{2_Y}$, **3**, $\mathbf{3_{Zn}}$ and $\mathbf{3_Y}$

	dc field	Orbach		Raman		QTM
Comp.	kOe	U_{eff} (K)	τ_0 (s)	C (s^{-1} K^{-n})	n	τ_{QTM} (s)
1	2.5	9.2 (FR)	6.4×10^{-7}			
		66.9 (SR)	1.2×10^{-7}			
$\mathbf{1_Y}$	2.5	46.8 (FR)	2.6×10^{-10}	285.4	2.04	
		94.0 (SR)	1.6×10^{-8}			
2	0	261.0	2.1×10^{-9}			
	1	342.4	2.4×10^{-10}	4.9×10^{-4}	5.11	
$\mathbf{2_Y}$	1	326.7	1.5×10^{-10}	1.0×10^{-4}	5.64	
3	2.5	203.0	1.4×10^{-8}	9.8	1.61	
$\mathbf{3_{Zn}}$	0	347.2	9.0×10^{-11}	0.052	3.86	1.2×10^{-3}
	2.5	334.8	2.4×10^{-10}	1.0×10^{-4}	5.65	
$\mathbf{3_Y}$ bis(CoY)	1.5			588.5 (FR)	2.59	4.9×10^{-4}
$\mathbf{3_Y}$ (CoDy)(CoY)		209.1 (SR)	6.0×10^{-9}			

Magnetically diluted samples were also studied to avoid possible intra- or intermolecular dipolar Dy···Dy interactions that may contribute to QTM. At zero applied dc field, the dynamic behaviour of $\mathbf{1_Y}$ is very similar to that of **1** under an external field of 1 kOe (Fig. S20†) in terms of SR, whereas FR appears to be hidden by a strong QTM. Therefore, magnetic dilution does not completely suppress QTM, but it is sufficient to trigger the SMM behaviour of the SR process. We repeated the measurements for $\mathbf{1_Y}$ under the same optimal external field as for **1** (2.5 kOe, Fig. S22†). Again, FR and SR processes were individually analysed by choosing the appropriate temperature range in $\chi''_M(\nu)$ curves. The temperature dependence of the relaxation times for the FR process was fitted to a combination of Raman and Orbach processes, whereas a single Orbach mechanism was considered for the SR process (Fig. 4). The corresponding magnetic parameters are given in Table 1. The analysis with CCFIT is shown in Fig. S27,† where consistent results are displayed.

The simultaneous appearance of two sets of maxima in the $\chi''_M(T)$ and $\chi''_M(\nu)$ plots may be due to (i) the presence of intra- or intermolecular interactions,[27,28] (ii) the emergence of novel relaxation mechanisms due to the presence of an external magnetic field,[11] or (iii) the coexistence of two crystallographically independent Dy^{III} ions,[29] although it is known that even a unique type of Dy^{III} ion can show two maxima.[30] We have ruled out the first hypothesis, since $\mathbf{1_Y}$ still exhibits two maxima. Based on the strategic rules of ligand field design proposed by Rinehart and Long[5] for oblate ions such as Dy^{III}, axial ligand fields are optimal for stabilizing higher M_J states. Therefore, when donor atoms with higher electron density are located in opposite positions in the Dy^{III} coordination sphere, the ligand field ensures the formation of an axial ground state. Thus, we conclude that the molecule that owns an acetate group as a chelating ligand provides better axiality of the ground state of the Dy^{III} ion than the one that contains a second nitrate (acetates provide more electron density than nitrates, as will be discussed later in the computational part). In view of this, we associate FR to the molecule possessing two chelate nitrates (**1A**), whereas SR is attributed to the molecule with acetate as a chelate (**1B**).

Compound **2** behaves like a zero-field SMM, displaying temperature- and frequency-dependent maxima in the ac susceptibility plots (Fig. 5 and Fig. S28 and S29†) below 28 K. The long tails below the maxima at low temperatures indicate the presence of QTM. Relaxation times were extracted from the 17.2–27.6 K temperature range (Fig. 5, top). Although the curvature of the Arrhenius plot at intermediate/low temperatures suggests that other relaxation mechanisms besides Orbach take place, it was not possible to obtain a reasonable fit (namely, combinations of Orbach + Raman and/or QTM were attempted). Considering the foregoing, only the linear part of the high temperature regime was fitted giving the values of U_{eff} and τ_0 given in Table 1.

With the aim of qualitatively investigating the influence of field and dilution on QTM, both quenching techniques were applied. For this purpose, we analysed the dynamic magnetic

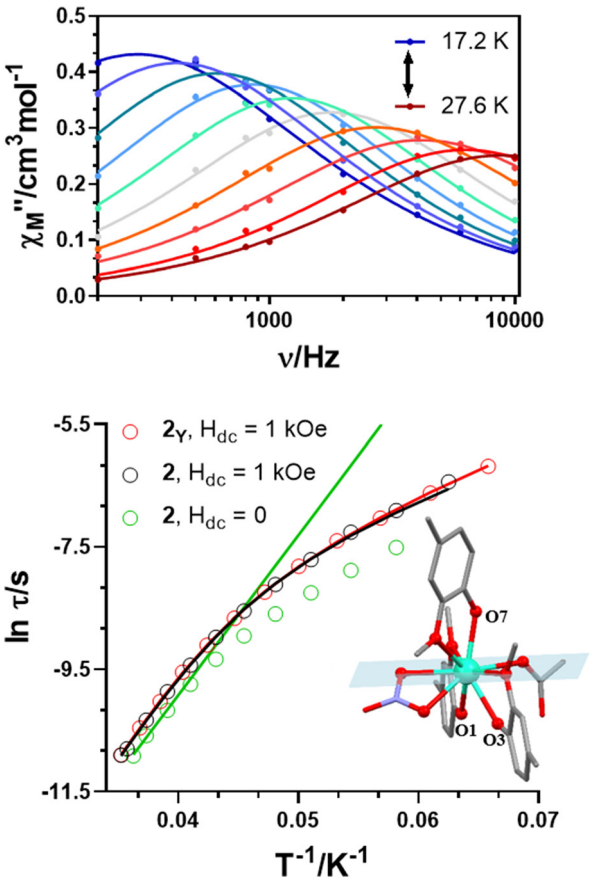

Fig. 5 Variable-temperature frequency dependence of the χ''_M signal under zero applied field for **2** (top panel). Arrhenius plots for relaxation times for **2**–$\mathbf{2_Y}$ under different experimental conditions (bottom panel). The solid lines represent the best fits. Inset: reduced fragment of **2**.

properties of **2** and $\mathbf{2_Y}$ under an optimum external magnetic field of 1 kOe (Fig. S31 and S32†). The fact that the QTM is gradually quenched is evidenced by the decrease of the tails in the $\chi''_M(T)$ plots (Fig. S34 and S38†). Consequently, the relaxation times become longer in the studied temperature range. On this occasion, we were able to fit the temperature dependence of the relaxation times for **2** and $\mathbf{2_Y}$ with the simultaneous occurrence of Orbach and Raman processes (Fig. 5, bottom). The best fit parameters are summarized in Table 1.

Despite the fact that the coordination environment of **2** is very similar to that of **1**, the replacement of the second nitrate (or chelating acetate) with phenoxido and methoxy groups remarkably improves its SMM behaviour. This is because the donor oxygen atoms belonging to the phenoxide groups have the shortest Dy–O distances and the highest electron density, and are located in opposite positions in the Dy^{III} coordination sphere: on one side O7, on the opposite side O1 and O3, belonging to the phenoxido groups connecting Zn^{II} and Dy^{III} ions. This arrangement of the shortest Dy–O bonds (Fig. 5 bottom, inset) creates a rather strong ligand field contributing to the axiality of the ground state of Dy^{III} ions[31,32] with the anisotropy axis passing near the Dy–O7 bond and between the

Dy–O1 and Dy–O3 directions, which agrees well with *ab initio* calculations (*vide infra*). Furthermore, the strong axiality is accompanied by a weak equatorial ligand field, since nitrate, carboxylate, and methoxy groups exhibit larger Dy–O distances and lower electronic densities on oxygen atoms than phenoxido groups; hence, they generate weaker fields. Thus, the serendipitous formation of such a coordination environment in **2**, caused by the coordination of the succinate connector, is suitable for enhancing the magnetic anisotropy of the trivalent dysprosium ion.

To elucidate the effect of replacing in **2** the Zn^{II} ion with the paramagnetic and anisotropic Co^{II} ion on the SMM properties, its related heterometallic tetranuclear bis(CoDy) system **3** was prepared. This compound does not show any maxima in the $\chi'_M(T)$ and $\chi''_M(T)$ plots at zero dc field (Fig. S10†), which could be attributed to the weak exchange and/or dipolar Co–Dy interactions operating in this compound (see the section on theoretical studies). These interactions could favour the fast QTM relaxation process. Nevertheless, it is known from the literature that some 3d–4f systems, where both metal cations are paramagnetic, exhibit improved SMM properties compared to systems in which the 3d ion is diamagnetic.[14] In such systems, the anisotropy axes of both ions are collinear, and relatively large exchange interactions slow down the relaxation processes and reduce the QTM. However, in many other 3d–4f systems, the introduction of a paramagnetic 3d ion had the opposite effect,[33] particularly when the above features are not fulfilled.

Measurements carried out at the optimal field of 2.5 kOe revealed two sets of well-defined maxima: the first in the range of 2.0–3.0 K and the second in the range of 12.0–27.0 K (Fig. S45†). However, the first set shows a low frequency dependence of the maxima with little or no temperature shift from 60 to 10 000 Hz. To better evaluate this effect, the Mydosh parameter ϕ was calculated using the formula $\phi = \Delta T_p/[T_p\Delta(\log f)]$, where T_p is the peak temperature and f is the frequency. The frequency shifts from 200 to 10 000 Hz (we discarded the 60 Hz curve due to the evident mixing of both maxima) gave a value of $\phi = 0.09$, which corresponds to glass-like behaviour.[34] High temperature relaxation, on the contrary, demonstrates a noticeable frequency dependence, which is consistent with SMM behaviour. Frequency-dependent out-of-phase susceptibility curves were fitted over the temperature range of 14.4–26.4 K using the generalized Debye model giving the relaxation time for each temperature (Fig. 6).

The curvature of the data in the Arrhenius plot, as well as the relatively large values of α extracted from the Cole–Cole plots, prompted us to fit the temperature dependence of the relaxation time using the combined Orbach and Raman relaxation paths (eqn (1)), which resulted in the set of parameters given in Table 1. Compared to the U_{eff} obtained for **2**, the barrier height is noticeably lower, but agrees well with the energy of the second excited exchange-coupled doublet (see the computational part). It is noteworthy that the low-temperature set of maxima can presumably be associated with relaxation through the first excited exchange doublet, which involves a very low energy barrier in agreement with the maxima at extremely low temperatures.

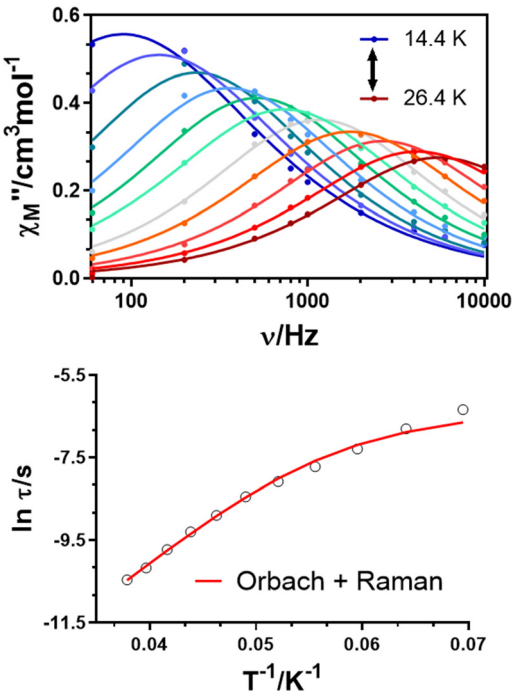

Fig. 6 Variable-temperature frequency dependence of the χ''_M signal under 2.5 kOe applied field for **3** (top panel). Arrhenius plot for relaxation times considering the simultaneous presence of Orbach and Raman mechanisms (bottom panel).

With the aim of disclosing the effect of magnetic dilution on the dynamic magnetic properties of **3**, we prepared two isostructural derivatives, namely $\mathbf{3_{Zn}}$ and $\mathbf{3_Y}$, by individually diluting Co^{II} ions with Zn^{II} or Dy^{III} ions with Y^{III}, respectively. These compounds contain 1 : 10 Co : Zn and Dy : Y, respectively (see Table S2† for ICP-MS results). Estimates show that the crystal structure of $\mathbf{3_{Zn}}$ is dominated (82.63%) by bis(ZnDy) (**2**), there are significantly fewer (16.53%) (ZnDy)(CoDy) complexes, as well as a small amount (0.83%) of bis(CoDy) (**3**). Therefore, it is not surprising that $\mathbf{3_{Zn}}$ behaves like a zero-field SMM, as seen in Fig. 7 and Fig. S47 and S48.† Below 28.0 K, a thermally activated relaxation process comparable to that exhibited by **2** occurs, consistent with the predominant contribution of bis(ZnDy) to the structure. The long tails appearing at low temperatures below the maxima indicate a pronounced QTM contribution (Fig. S48†). The temperature dependence of the relaxation time (Fig. 7) was fitted assuming the simultaneous presence of the Orbach, Raman and QTM mechanisms (eqn (1)) with the set of best-fit parameters collected in Table 1. The values related to Orbach and Raman mechanisms are comparable to those obtained for **2** or $\mathbf{2_Y}$ under an external magnetic field. When the same measurements were repeated under an external magnetic field of 2.5 kOe (field selected according to the field dependent measurements carried out for **2** and **3**), the QTM was successfully quenched (Fig. S52†). The small tails observed in Fig. S51 and S52† at very low temperature

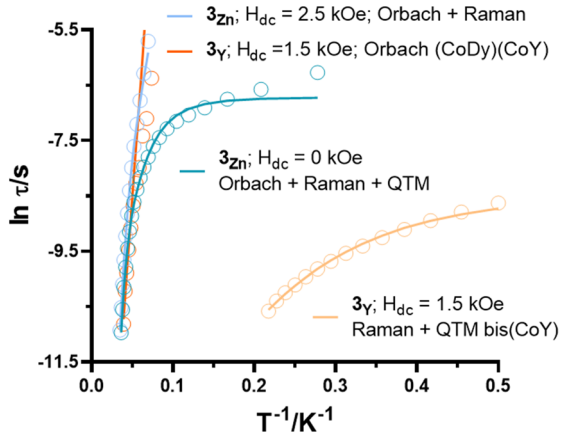

Fig. 7 Arrhenius plots for the relaxation times and their fitting when considering the simultaneous presence of several mechanisms (experimental conditions are summarized in the Figure).

may be due to the residual QTM contribution and/or a relatively small number of exchange-coupled (ZnDy)(CoDy) molecules within the material. The absence of clear maxima at very low temperatures in the $\chi''_M(T)$ plot even at the highest frequency is consistent with a small energy gap between the ground and first excited exchange-coupled states. The relaxation times in the high temperature region were fitted by taking into account the combination of Orbach and Raman processes in eqn (1), affording the values indicated in Table 1. Almost identical values were obtained for **2** under an external magnetic field (Table 1).

In the case of $\mathbf{3_Y}$, the situation is reversed with respect to $\mathbf{3_{Zn}}$, and the dominant species in the structure is bis(CoY), followed by a substantially smaller amount of (CoDy)(CoY) and an overwhelming minority of bis(CoDy) (**3**). It should be noted that in the bis(CoY) species, the Co^{II} ions have a square-pyramidal coordination environment, for which slow relaxation at zero-field is rarely observed.[35,36] This fact, along with the lack of slow relaxation in **3**, explains why $\mathbf{3_Y}$ does not exhibit out-of-phase ac susceptibility peaks at zero-field (Fig. S55†). When an external magnetic field of 1 kOe is applied, the temperature dependence of the out-of-phase ac susceptibility exhibits two maxima: the first below 4.0 K and the second (much less intense) below 26.0 K (Fig. S55†). We attribute the former to the relaxation of Co^{II} ions (for square-pyramidal Co^{II} complexes, field-induced χ''_M peaks usually appear below 6 K[35,36]), while the latter corresponds to the exchange coupled Co–Dy system. Field-dependent measurements of $\chi''_M(\nu)$ were carried out for the two individual processes at 2.0 K and 22.6 K. The field dependence of the relaxation times, obtained from fitting the $\chi''_M(\nu)$ data with a generalized Debye model, allowed us to conclude that an external magnetic field of 1.5 kOe was adequate for slowing down the relaxation times for both processes (Fig. S56–S59†).

When measuring the ac dynamic magnetic properties of $\mathbf{3_Y}$ under the optimal field, the set of maxima at low temperature becomes frequency-dependent, and the Mydosh parameter ϕ = 1.0 is consistent with the SMM behaviour (Fig. S61†). The temperature dependence of the relaxation time was fitted taking into account both Raman and QTM processes (eqn (1)). The best fit afforded the set of parameters shown in Table 1. Accounting for three mechanisms (including also the Orbach process) did not give any reasonable fit. The presence of multiple relaxation paths is in agreement with the large α values (0.18 (2.0 K)–0.36 (4.6 K)). In the case of the slower relaxation process, a small proportion of (CoDy)(CoY) species in the structure leads to a weaker and noisier signal. We attempted to fit the relaxation times considering the simultaneous presence of the Orbach and Raman processes because α values (0.46 and 0.12 at 13.6 and 25.6 K, respectively) indicate the participation of several mechanisms. However, the fit did not afford any reasonable result. Thus, only the Orbach process was used to fit data for the high temperature regime, yielding the parameters gathered in Table 1. Note that the barrier height is almost identical to that found for **3**, which is consistent with relaxation through the second excited state of the exchange-coupled Co–Dy system (see details in the Theoretical studies section).

Last but not least, Fig. S66† displays all the Arrhenius plots involving data for pure **2** and **3** and for their diluted counterparts. As can be seen from this figure, compounds containing the (CoDy)(CoY) ($\mathbf{3_Y}$) or bis(CoDy) (**3**) species within the structure exhibit lower energy barriers and faster relaxation times than those containing the bis(ZnDy) (**2**), (ZnDy)(ZnY) ($\mathbf{2_Y}$) or (ZnDy)(CoDy) ($\mathbf{3_{Zn}}$) systems. This fact will be confirmed by *ab initio* calculations, which are extensively discussed in the "Theoretical studies" section.

As it can be observed in Table 1, τ_0 values decrease as the U_{eff} values increase. This trend is not unexpected because τ_0 is expected to be proportional to $|D|^{-3}$ whereas U, the thermal energy barrier, is proportional to D.[37]

Hysteretic behavior

We performed the magnetization hysteresis loop measurements on powdered samples of **2**, $\mathbf{2_Y}$ and $\mathbf{3_{Zn}}$ at 2 K to confirm their SMM behaviour (Fig. S67†). For **2**, we used an average sweep rate of 7.7×10^{-3} T s^{-1} over the 0.44 to −0.63 T range and 8.8×10^{-3} T s^{-1} over the −0.44 to 0.63 T range. For $\mathbf{2_Y}$, an average sweep rate of 4.4×10^{-3} T s^{-1} was employed in the range of 0.50 to −0.50 T and −0.50 to 0.50 T. Finally, for $\mathbf{3_{Zn}}$, an average sweep rate of 7.0×10^{-3} T s^{-1} was used in the range of 0.55 to −0.55 T and −0.55 to 0.55 T (in all cases slower in low fields and faster in high fields). Even though these compounds exhibited butterfly-shaped hysteresis loops without any remnant magnetization at zero field, a larger opening was observed for $\mathbf{2_Y}$ in agreement with partial quenching of QTM by diamagnetic dilution. This is consistent with the differences observed in the QTM regimes in the $\chi''_M(T)$ plots.

To better understand the magnetization dynamics, the magnetization curves for the most promising compounds (**2**, $\mathbf{2_Y}$, **3** and $\mathbf{3_{Zn}}$) were measured in a full cycle pulsed magnetic field (Fig. 8).[38] These measurements were carried out at 0.4 K with a maximum field of 10.4 T. They allowed us to observe

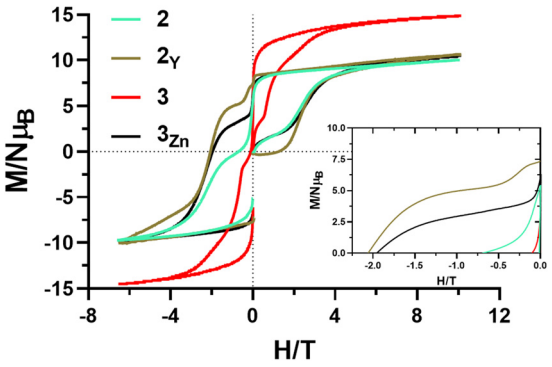

Fig. 8 Pulsed-field magnetization curves at a maximum field of 10.4 T and temperature of 0.4 K for **2**, $\mathbf{2_Y}$, **3** and $\mathbf{3_{Zn}}$. Inset: Loop expansion to compare coercive fields. Note that the values for $\mathbf{2_Y}$ have been normalized to give comparable loops.

much larger hysteresis loops, because the sweep rates of 4.2×10^3 T s^{-1} are extremely fast compared to what we used in the continuous field measurements (Fig. S67†). It is important to note that the field strength is not symmetrical in the positive and negative directions during the pulsing (Fig. S68†).

Let us first compare the hysteresis curves for **2** and **3**. The latter compound exhibits a butterfly-shaped hysteresis loop with a sharp magnetization reversal close to zero field and a very small (compared to **2**, $\mathbf{2_Y}$ and $\mathbf{3_{Zn}}$) coercive field of 0.14 T (Fig. 8). This behaviour is consistent with the fact that **3** exhibits neither slow magnetization relaxation at zero field, as indicated by ac measurements, nor hysteresis loops in dc measurements at much slower sweep rates. In contrast, compound **2**, even at zero field, shows a clear open loop with a relatively large coercive field of 0.75 T. This behaviour would be in line with both the slow relaxation at zero field observed in the ac measurements and the butterfly-shaped hysteresis loop obtained from continuous field measurements (Fig. S67†). Surprisingly, diamagnetically diluted $\mathbf{3_{Zn}}$ (or, in other words, compound **2**, doped with Co^{II}) displayed a larger hysteresis loop than **2** with a notably smaller QTM contribution at zero field (Fig. 8). In fact, the coercive field for $\mathbf{3_{Zn}}$ was estimated to be 2.0 T, which is more than twice that of **2**. Likewise, the remnant magnetization is slightly higher for the diluted compound (67.6% of the saturation values for $\mathbf{3_{Zn}}$ and 63.5% for **2**, respectively). For an unknown reason, pulse magnetization measurements indicate that a low concentration of Co^{II} replacing Zn^{II} ions improves the SMM properties. This is unexpected given the previous ac measurements (faster relaxation times for $\mathbf{3_{Zn}}$ than for **2**, see Fig. S69†) and the hysteresis loops measured in a continuous field (both compounds exhibit almost identical hysteresis loops). This astonishing behaviour of pulse magnetization is what we will try to explain in a future work by investigating doped versions of **2** with variable Co : Zn ratios.

Finally, we also studied compound $\mathbf{2_Y}$, which was synthesized to reduce intra- and intermolecular Dy···Dy interactions that could facilitate QTM (Fig. 8). Similar to what we observed in the ac measurements, the QTM is almost completely quenched, and the loop opening for the diluted $\mathbf{2_Y}$ counterpart is even larger than that for $\mathbf{3_{Zn}}$.

Theoretical studies

To better understand the dynamics of magnetization relaxation in the studied compounds, SA-CASSCF (state-averaged complete active space self-consistent field) calculations, followed by SO-RASSI (restricted active space state interaction) calculations, were performed for all binuclear fragments of compounds **1**–**3** (named **1′A**, **1′B**, **2′** and **3′**) with one paramagnetic ion using the geometries from the crystal structure data. For all these calculations, the OpenMolcas program was used (see the ESI†). It is worth noting that in **3**, diamagnetic Zn^{II} or Y^{III} ions replaced the paramagnetic Co^{II} or Dy^{III} ions, respectively. To calculate the magnetic properties of such complexes, we used the SINGLE_ANISO procedure implemented in Molcas.

As described above, compound **1** consists of molecules **1A** and **1B** where in each ZnDy unit, in addition to a nitrate chelating the Dy^{III} ion, there is a nitrate or acetate chelating ligand coordinated to the same Dy^{III} ion, respectively. *Ab initio* calculations demonstrate that completely different relaxation behaviour is expected for these counterparts. On the one hand, the ground Kramers doublet (KD) for **1′B** is almost pure Ising type (KD1: M_J = ±15/2, 98.6%; see Table S8†), while for **1′A** it is noticeably mixed (KD1: M_J = ±15/2, 83.8%; see Table S9†). In good agreement with this, the ground state KD for **1′B** has a g_{zz} value close to 20 (the ideal Ising ground state has $g_x = g_y = 0$ and $g_z = 20$ when using pseudospin $S_{eff} = 1/2$) and almost negligible g_{xx}/g_{yy} values (Table S10†). The strong axiality of the ground KD suppresses the QTM within this doublet state, since the matrix element of the transverse magnetic moment within the +1/−1 ground KD (0.004) is significantly smaller than the required threshold of 0.1 for an efficient relaxation mechanism (Fig. S70†).[39] This fact justifies why $\mathbf{1_Y}$ exhibits slow magnetic relaxation at zero applied dc field when the intermolecular interactions that facilitate QTM are suppressed (Fig. S20†).

On the other hand, the ground KD of **1′A** presents significant transverse anisotropy, with g_{xx}/g_{yy} values much higher than those for **1′B** (Table S11†). This factor, together with the mixed nature of the ground state wave function, results in a matrix element of the transverse magnetic moment within the ground KD of 0.23 (Fig. S71†), which indicates that the QTM relaxation within this KD is plausible. This explains why there is no zero-field SMM behaviour for this counterpart (Fig. S20†). In addition, we assume that both molecules (**1′A** and **1′B**) relax through the first excited KD when applying an H_{dc} field, since the matrix elements for the vertical and diagonal transitions (Orbach process) are large enough to allow the magnetization relaxation through these pathways. The experimentally and theoretically evaluated energy barriers are of 46.8 K and 46.0 K for **1A** and 94.0 K and 173 K for **1B**, respectively.

The improved properties of **1′B** compared to **1′A** can be easily rationalized by analysing the ligand field around the respective Dy^{III} ions. In the Dy^{III} coordination sphere of both units **1′A** and **1′B**, the oxygen atoms of the phenoxido groups

are located in neighbouring positions on the same side of Dy^{III}. They have the largest negative atomic charges among all other coordinated oxygen atoms (Tables S12 and S13†) and thus are expected to align the anisotropy axis along the Dy–$O_{phenoxido}$ directions. Consequently, the larger the negative charge on the opposite side from the phenoxido oxygen atoms in the Dy^{III} coordination sphere, the better the oblate like electron cloud of this ion will be stabilized. Given that the main difference between **1′A** and **1′B** is the chelate located just on the opposite side of the phenoxido donor atoms, it is expected that the group providing a larger negative charge will create a more suitable ligand field for higher ground state axiality and hence for improved SMM properties. Indeed, as evidenced by the calculated Mulliken charges (Tables S12 and S13†), chelating acetate in **1′B** has a significantly greater negative atomic charge on oxygen than nitrate in **1′A**, which accounts for the better SMM properties observed for **1′B**. Moreover, as expected, the easy axis in the **1′B** ground state passes through the middle of the phenoxides and through the acetate (Fig. S72†). In the case of **1′A**, the orientation of the easy-axis is largely influenced by the Zn–Dy bridging acetate (Fig. S73†), which also provides a large negative charge (Table S13†).

As evidenced by the results of dynamic magnetic studies of compounds **2** and **3** and their diluted counterparts, all of them can be divided into two groups depending on the energy barriers associated with high temperature data ($\chi''_M(T)$ maxima around 26 K). Under optimal external magnetic fields, **3** and $\mathbf{3_Y}$ display energy barriers of about 200 K, whereas **2**, $\mathbf{2_Y}$ and $\mathbf{3_{Zn}}$ show higher barriers, reaching values close to 350 K. These two sets of U_{eff} values are confirmed by theoretical calculations.

The relaxation dynamic in **2** and $\mathbf{2_Y}$ arises from the Zn–Dy units and therefore originates from a single Dy^{III} ion. The calculated energy level spectrum and anisotropic *g*-tensor values for **2′** are given in Tables S14 and S15,† while the computed relaxation mechanism is shown in Fig. 9. It is worth highlighting at this point that the calculated energy spectrum of the low-lying KDs for **2′** was confirmed by photoluminescence measurements (see below).

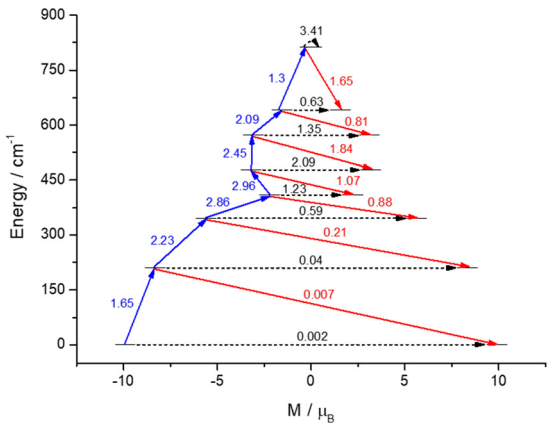

Fig. 9 Magnetization blocking barrier for **2′**. The exchange states are arranged according to the values of their magnetic moments. The arrows show the connected exchange states, and the numbers at each of them stand for the corresponding matrix element of the transverse magnetic moment.

The overwhelming contribution to the ground KD1 comes from the $M_J = \pm 15/2$ wavefunction (99.6%; Table S14†) and the *g* tensors are close to the ideal axial state (Table S15†). Hence, the slow relaxation of the magnetization under zero applied dc field observed for this compound is not surprising, since QTM within the ground state is significantly suppressed (the matrix element of the transverse magnetic moment within the ground state is 0.002, Fig. 9).

The following factors can contribute to magnetic relaxation through the first excited state (KD2): (i) significant transverse components of the *g* tensor in KD2, (ii) a non-negligible contribution of the $M_J = \pm 11/2$ wavefunction in KD2, and (iii) a considerable angle between the easy axes of KD1 and KD2 (14.4°; Table S16†). However, the matrix element of the transverse magnetic moment within KD2 is too small and magnetic relaxation through it may not be effective enough. Thus, magnetic relaxation through KD3, which is 469 K (326 cm^{-1}) above KD1, is quite plausible. The deviation between the calculated energy of KD3 and the experimental U_{eff} value of 342.4 K, could be due to the occurrence of relaxation through both the first and second excited states, *e.g.* KD2 and KD3.

As explained in the section concerning dynamic magnetic measurements, the good SMM magnetic properties of complex **2** arise from the appropriate ligand field. The calculation of the Mulliken atomic charges (Table S17†) supports this hypothesis, as it has been demonstrated that the oxygen atoms of the three phenoxido groups (two on one side and one on the other) have the largest negative atomic charges, while the equatorial positions are occupied by oxygen atoms with a smaller negative charge. This way, the orientation of the theoretically calculated anisotropy axis is defined by the more negatively charged O7 atom with the shortest Dy–O distance, as depicted in Fig. S74.†

Regarding compound **3**, it has been suggested elsewhere that the ferromagnetic exchange interaction between Co^{II} and Dy^{III} is the reason for its lack of SMM behaviour at zero field. In fact, calculations of the single ion anisotropy of Co^{II} and Dy^{III} ions in **3** ($\mathbf{3'_{Zn}}$ for ZnDy and $\mathbf{3'_Y}$ for CoY, respectively), as well as the proposed mechanisms of their relaxation (Tables S18–S20 and Fig. S75–S78†) cannot fully rationalize the absence of slow relaxation in this compound. In order to support the involvement of the exchange coupling in the magnetization relaxation of **3**, we used the POLY_ANISO program (see the ESI†), which takes into account both the dipole–dipole interaction and anisotropic exchange coupling within the Lines model to fit the experimental susceptibility using the results of calculations for dinuclear complexes containing only paramagnetic Dy^{III} or Co^{II} ions. The estimated exchange coupling parameter between Co^{II} and Dy^{III} ions extracted from the fitting procedure was $J = +0.48$ cm^{-1}. As seen in Fig. 3, the best-fit curve is in good agreement with the experimental one. The calculated low-lying exchange spectrum and the corresponding tunnelling gaps and g_{zz} values for **3′** are given in

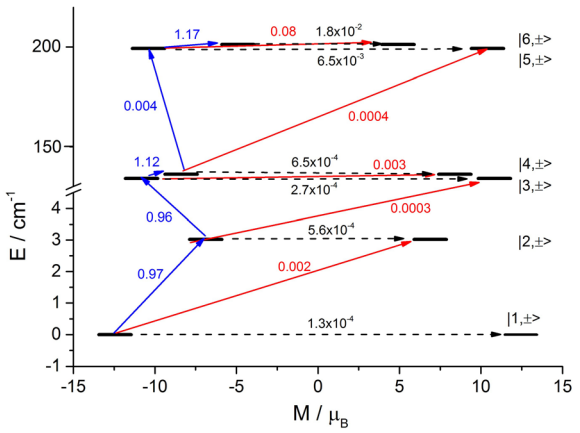

Fig. 10 Magnetization blocking barrier for **3′**. The exchange states are arranged according to the values of their magnetic moments. The horizontal black dashed arrows show the tunneling transitions within each doublet state (the black numbers are the corresponding tunneling gaps, ΔE_{tun}, in cm^{-1}), whereas red and blue arrows show the spin–phonon transitions (the numbers are the matrix elements of the transverse magnetic moment between the corresponding states).

Table S21,† whereas Fig. 10 represents the corresponding computed relaxation mechanism. The ΔE_{tun} for the exchange coupled ground doublet (1.3×10^{-4} cm^{-1}) is similar to that observed for other 3d-Dy systems with QTM relaxation in the ground state.[40] It seems that in such exchange coupled systems, ΔE_{tun} values less than $\sim 10^{-6}$ cm^{-1} are required to avoid QTM relaxation in the ground state. Moreover, intermolecular and hyperfine interactions, which were not considered in the calculated relaxation mechanism, could also contribute to QTM in the ground state. The first three excited states possess relatively high ΔE_{tun} in the range of 2.7×10^{-4}–6.5×10^{-4} cm^{-1} (Table S21†), which suggests that magnetic relaxation through these states is achievable.

As indicated elsewhere, when an external magnetic field is applied, **3** displays a set of maxima at very low temperatures, which has been attributed to spin-glass behaviour, whereas $\mathbf{3_{Zn}}$ shows a set of tails corresponding to a relaxation process with maxima occurring below 2 K. This incipient relaxation process, which would be hidden by the spin-glass behaviour in **3**, could be tentatively assigned to the relaxation through the first excited state with a U_{calc} value of 3.0 cm^{-1}. Alternatively, since the magnetic energy for an applied dc field of 2.5 kOe is close to the energy calculated for the first excited state, the magnetic field can overcome this energy barrier, and then relaxation can occur directly through the next excited states. The second set of maxima, appearing near 27 K on the $\chi''_M(T)$ plots of **3** and $\mathbf{3_Y}$, can be associated with relaxation through almost degenerate second and third excited doublets with a calculated energy gap of 192.8 K (134 cm^{-1}) and 195.8 K (136 cm^{-1}), respectively. These U_{cal} values are in good agreement with the experimentally estimated U_{eff} values of about 200 K for **3** and $\mathbf{3_Y}$. Thus, magnetic relaxation dynamics of these compounds can be well explained by considering the exchange coupled system.

Photoluminescence properties

In view of the exciting magnetic properties of compounds **1** and **2**, we were encouraged to study their photoluminescence properties as potential multifunctional compounds. As stated in the Introduction section, the Dy^{III}-based compounds exhibit emission in the visible range.

Excitation spectra were collected at room temperature by monitoring the most intense emission line at 578 nm (Fig. S80† and Fig. 11 for **1** and **2**, respectively). The broad bands over 300 nm are attributed to the n → π* and π → π* transitions of H_4L, but are followed by even stronger narrow bands related to lanthanide centred f–f transitions, meaning that the antenna effect is not so effective in these cases. Nevertheless, the characteristic Dy^{III} emission bands dominate in the emission spectra recorded at low and room temperatures (monochromatic laser excitation with λ_{ex} = 325 nm, Fig. S80 and S81† for **1** and Fig. 11 and Fig. S82† for **2**, respectively). In particular, the blue and yellow emission lines (centred at 482 and 579 nm, respectively) corresponding to the $^4F_{9/2} \rightarrow {}^6H_{15/2}$ and $^4F_{9/2} \rightarrow {}^6H_{13/2}$ transitions are the most intense, although there are other weaker emission bands as well as ligand fluorescence (350–550 nm range, especially for **2**). The presence of a dominant $^4F_{9/2} \rightarrow {}^6H_{13/2}$ transition is in good agreement with the low symmetry environment of the Dy^{III} ion, as follows from the description of the crystal structure.[41]

In addition to the interesting emission properties, these measurements provide information about the electronic structure of the ground multiplet. For each system, the 482 nm centred emission line is actually a multiplet in which relaxation occurs through the $^4F_{9/2}$ emitting state to each of the KDs within the $^6H_{15/2}$ ground multiplet. It should be noted that, at room temperature, the emission bands consist not only of transitions between the lowest emitting KD and all KDs arising from the ground state of the f-metal cation (zero-phonon bands), but also hot-bands and vibronic side bands are usually present. Therefore, the interpretation of the multiplet becomes more complicated. In fact, it is not easy to assign

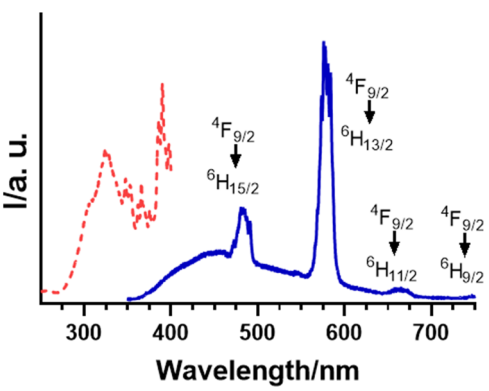

Fig. 11 Solid state photoluminescence excitation (dashed red line) and emission (blue line) spectra for compound **2**. The excitation spectrum was recorded at room temperature, whereas the emission spectrum was recorded at 10 K.

individual transitions to theoretically calculated KDs for the room temperature spectra (Fig. S83 and S84†). However, the resolution of the spectra improves notably when measuring them at low temperature, when single transitions can be distinguished by the structure shown in the emission bands. In fact, for complex **2**, an extraordinary agreement was found between the theoretically calculated energy splitting of the ground $^6H_{15/2}$ state and the 482 nm centred emission band recorded at 10 K, as depicted in Fig. 12. More specifically, the *ab initio* calculated total energy splitting of KDs arising from the ground $^6H_{15/2}$ state is 750 cm^{-1}, which agrees well with the value of 785 cm^{-1} found in the photoluminescence measurement. Moreover, the energy differences between the ground and excited KDs fit well with the observed emission lines confirming the validity of the calculated values. Although we have attempted a similar approach for compound **1**, the fact that there are two distinct compounds (**1A** and **1B**) within the same crystal structure complicates the interpretation of the spectrum as observed in Fig. S85.†

To further characterize the photoluminescence performance of the samples, we measured the emission decay curves at room and low temperatures. To start with, the emission lifetime of the Dy^{III} centres was estimated by measuring the decay curves at room temperature focusing at the main emission band (λ_{em} *ca.* 579 nm). These curves were properly fitted by the exponential expression ($I_t = A_0 + A_1\exp(t/\tau_1) + A_2\exp(t/\tau_2)$) with two and one components for **1** and **2**, respectively, which is consistent with the fact that compound **1** contains two crystallographically independent Dy^{III} centres in the structure. The best fitting results yield very similar lifetimes for both compounds ($\langle\tau\rangle$ = 20.3 μs for **1** and 20.6 μs for **2**, see Fig. S86 and S87†), which are of the same order as those measured for Dy^{III}-based centres with similar coordination environments.[10,42,43] These emissions are comparatively longer than those of the ligand (τ of *ca.* 3 ns) and are practically temperature independent, showing no noticeable increase when the samples are cooled to 10 K. To complete the characterization of the photoluminescence properties, the absolute emission quantum yield (QY) was measured for both compounds, reaching a value of 2.5% and 1.8% for **1** and **2**, respectively. Although the reason for the higher QY in **1** may be related to several facts (arrangement of the L around the Dy^{III} centre, quenching by the solvent molecules), the presence of an additional chelating acetate in **1B** could be a possible cause. As discussed earlier, acetate ligands bring higher charge transfer to Dy^{III} than nitrate groups and hence may improve the antenna effect and provide brighter emission by the lanthanide cation.

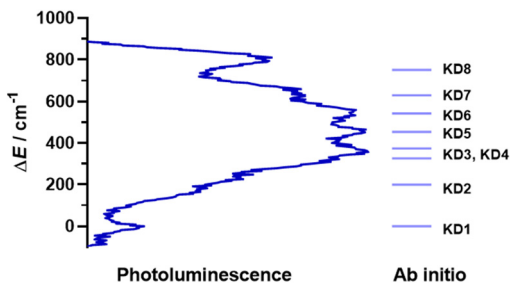

Fig. 12 The $^4F_{9/2} \rightarrow {}^6H_{15/2}$ emission band of compound **2** recorded at 10 K in the relative energy scale (left) and energies of Kramers doublets according to *ab initio* calculations (right).

Conclusions

We have reported here the structural, magnetic and photoluminescence properties as well as theoretical calculations for two tetranuclear bis(ZnDy) complexes with a novel di(compartmental) ligand, which exhibit an open (**1**) or closed (**2**) structure depending on the nature of the carboxylate bridging ancillary ligand. For further magnetic studies, an isostructural counterpart of **2**, bis(CoDy) (**3**) as well as diamagnetically diluted versions of these compounds were also synthesized.

Based on the experimental and computational results, we conclude that fragment **1B** within **1** displays a more appropriate ligand field resulting in greater axiality of the ground state of the oblate Dy^{III} ion. This is because the oxygen atoms of the chelating acetate group in **1B**, located in the position opposite to the bridging phenoxido groups, have greater negative charge than the oxygen atoms of the bidentate nitrate in **1A**. Compound **1** does not exhibit slow magnetic relaxation at zero field, but slow relaxation at zero field is observed in the magnetically diluted $\mathbf{1_Y}$. Theoretical calculations indicated that the zero-field SMM behaviour of $\mathbf{1_Y}$ is due to the presence of the **1B** fragment, but not **1A**. Under an optimum external magnetic field, U_{eff} values of 46.8 K and 94.0 K were determined for **1A** and **1B**, respectively, in the magnetically diluted complex $\mathbf{1_Y}$ (*ab initio* calculations predict 46 K and 173 K for the energies of the first excited KDs of **1A** and **1B**, respectively).

Complex **2** showed prominent zero-field SMM behaviour and butterfly-shaped hysteresis loops. The experimentally estimated energy barrier (U_{eff} ~ 340 K) falls in between the *ab initio* calculated energies of the first (KD2) and second (KD3) excited Kramers doublets (at 286 and 469 K, respectively), which can be explained by simultaneous relaxation through both of these KDs. The good performance of **2** is due to the specific and not pre-defined coordination environment around the Dy^{III} ion, in which three phenoxide groups provide improved axiality to the system. In **3**, the CoDy fragments exhibit weak ferromagnetic coupling, which is responsible for the QTM in the ground state that causes a lack of slow relaxation at zero field, as revealed by the theoretical calculations. The calculated exchange coupled electronic structure displays three excited non-Kramers doublets at 4.3, 192.8 and 195.8 K, respectively, through which relaxation can occur. At H_{dc} = 2.5 kOe, only relaxation through the second/third excited states was observed (experimentally estimated U_{eff} = 203.0 K), while at low temperatures an unexpected glass-like feature was detected that could hide the relaxation through the first excited state. Further studies carried out on diluted $\mathbf{3_Y}$ and $\mathbf{3_{Zn}}$ counterparts provided very valuable information. We were able to assign individual relaxation mechanisms for the bis(CoY)

and (CoDy)(CoY) fragments in $\mathbf{3_Y}$, whereas for $\mathbf{3_{Zn}}$ we found relaxation through the first excited non-Kramers doublet of CoDy and an additional relaxation related to the ZnDy units.

Finally, the multifunctional nature of **1** and **2** was demonstrated by photoluminescence measurements. Indeed, characteristic emission bands associated with the Dy^{III} ion were observed even at room temperature. Furthermore, for **2** we were able to relate the low-temperature narrow emission band to the *ab initio* calculated electronic structure of the system, demonstrating the suitability of the calculation methodology used.

Author contributions

A. Z.-L. and X. L. P. synthesized and characterized the materials. I. F. D.-O. and H. N. performed the pulse magnetization measurements. J. C. analysed the photoluminescence properties. N. P. G. and A. A. D. carried out the theoretical studies. A. L.-O. analysed the dynamic magnetic properties. A. R.-D. obtained and solved the SCXRD data. J. M. S. and E. C. conceived the idea, acquired the financial support and reviewed/edited the manuscript. A. Z.-L. analysed the data and wrote the original draft. All authors discussed the results and commented on the manuscript.

Conflicts of interest

There are no conflicts to declare.

Acknowledgements

This work was developed within the scope of the projects given by the Spanish Ministry of Science, Innovation and Universities (MCN/AEI/FEDER, UE) (PGC2018-102052-A-C22, PGC2018-102052-B-C21, MCIN/ AEI /10.13039/501100011033/ FEDER "Una manera de hacer Europa"), the University of the Basque Country (GIU 20/028), Gobierno Vasco/Eusko Jaurlaritza (IT1755-22), Red Guipuzcoana de Ciencia, Tecnología e Innovación (FA385/2023, DG23/16) and Junta de Andalucía (FQM-195, FQM-394, A-FQM-172-UGR18 and B-FQM-734-UGR20 and ProyExcel_00386). This work was partly supported by GIMRT and ICC-IMR programs of the Institute for Materials Research, Tohoku University. HN acknowledges the support by KAKENHI19H00647. ALO acknowledges the financial support from the grants PID2021-122613OB-I00 funded by MCIN/AEI/ 10.13039/501100011033 and PJUPNA2020 from Universidad Pública de Navarra. NPG and AAD acknowledge the Russian Science Foundation (project no. 22-13-00077) for financial support of the computational part of this work.

References

1 A. Zabala-Lekuona, J. M. Seco and E. Colacio, *Coord. Chem. Rev.*, 2021, **441**, 213984.
2 M. Affronte, *J. Mater. Chem.*, 2009, **19**, 1731–1737.
3 E. Coronado, *Nat. Rev. Mater.*, 2020, **5**, 87–104.
4 F. S. Guo, B. M. Day, Y. C. Chen, M. L. Tong, A. Mansikkamäki and R. A. Layfield, *Science*, 2018, **362**, 1400–1403.
5 J. Rinehart and J. Long, *Chem. Sci.*, 2011, **2**, 2078–2085.
6 Y. S. Ding, N. F. Chilton, R. E. P. Winpenny and Y. Z. Zheng, *Angew. Chem., Int. Ed.*, 2016, **55**, 16071–16074.
7 J. Liu, Y. C. Chen, J. L. Liu, V. Vieru, L. Ungur, J. H. Jia, L. F. Chibotaru, Y. Lan, W. Wernsdorfer, S. Gao, X. M. Chen and M. L. Tong, *J. Am. Chem. Soc.*, 2016, **138**, 5441–5450.
8 Y. C. Chen, J. L. Liu, L. Ungur, J. Liu, Q. W. Li, L. F. Wang, Z. P. Ni, L. F. Chibotaru, X. M. Chen and M. L. Tong, *J. Am. Chem. Soc.*, 2016, **138**, 2829–2837.
9 C. A. P. Goodwin, F. Ortu, D. Reta, N. F. Chilton and D. P. Mills, *Nature*, 2017, **548**, 439–442.
10 A. Zabala-Lekuona, J. Cepeda, I. Oyarzabal, A. Rodríguez-Diéguez, J. A. García, J. M. Seco and E. Colacio, *CrystEngComm*, 2017, **19**, 256–264.
11 E. Echenique-Errandonea, A. Zabala-Lekuona, J. Cepeda, A. Rodríguez-Diéguez, J. M. Seco, I. Oyarzabal and E. Colacio, *Dalton Trans.*, 2019, **48**, 190–201.
12 E. Colacio, *Top. Organomet. Chem.*, 2019, **64**, 101–161.
13 A. Upadhyay, S. K. Singh, C. Das, R. Mondol, S. K. Langley, K. S. Murray, G. Rajaraman and M. Shanmugam, *Chem. Commun.*, 2014, **50**, 8838–8841.
14 S. K. Langley, D. P. Wielechowski, V. Vieru, N. F. Chilton, B. Moubaraki, B. F. Abrahams, L. F. Chibotaru and K. S. Murray, *Angew. Chem., Int. Ed.*, 2013, **52**, 12014–12019.
15 S. K. Singh, M. F. Beg and G. Rajaraman, *Chem. – Eur. J.*, 2016, **22**, 672–680.
16 L. Ungur, M. Thewissen, J. P. Costes, W. Wernsdorfer and L. F. Chibotaru, *Inorg. Chem.*, 2013, **52**, 6328–6337.
17 P. Comba, M. Enders, M. Großhauser, M. Hiller, D. Müller and H. Wadepohl, *Dalton Trans.*, 2016, **46**, 138–149.
18 J. C. G. Bünzli, *Chem. Rev.*, 2010, **110**, 2729–2755.
19 S. V. Eliseeva, M. Ryazanov, F. Gumy, S. I. Troyanov, L. S. Lepnev, J.-C. G. Bünzli and N. P. Kuzmina, *Eur. J. Inorg. Chem.*, 2006, 4809–4820.
20 M. Bender, P. Comba, S. Demeshko, M. Großhauser, D. Müller and H. Wadepohl, *Z. Anorg. Allg. Chem.*, 2015, **641**, 2291–2299.
21 M. Llunell, D. Casanova, J. Cirera, P. Alemany and S. Alvarez, *SHAPE v2.1*, Barcelona, Spain, 2013.
22 K. R. Meihaus and J. R. Long, *J. Am. Chem. Soc.*, 2013, **135**, 17952–17957.
23 J. Luzon, K. Bernot, I. J. Hewitt, C. E. Anson, A. K. Powell and R. Sessoli, *Phys. Rev. Lett.*, 2008, **100**, 247205.
24 K. R. Meihaus, J. D. Rinehart and J. R. Long, *Inorg. Chem.*, 2011, **50**, 8484–8489.
25 R. J. Blagg, L. Ungur, F. Tuna, J. Speak, P. Comar, D. Collison, W. Wernsdorfer, E. J. L. McInnes, L. F. Chibotaru and R. E. P. Winpenny, *Nat. Chem.*, 2013, **5**, 673–678.
26 D. Reta and N. F. Chilton, *Phys. Chem. Chem. Phys.*, 2019, **21**, 23567–23575.

27 A. Arauzo, A. Lazarescu, S. Shova, E. Bartolomé, R. Cases, J. Luzón, J. Bartolomé and C. Turta, *Dalton Trans.*, 2014, **43**, 12342–12356.
28 A. A. García-Valdivia, A. Zabala-Lekuona, A. Goñi-Cárdenas, B. Fernández, J. A. García, J. F. Quílez del Moral, J. Cepeda and A. Rodríguez-Diéguez, *Inorg. Chim. Acta*, 2020, **509**, 119687.
29 C. Shi, R. Nie, X. Yao, S. Fan, G. An, Y. Dong and G. Li, *RSC Adv.*, 2017, **7**, 49701–49709.
30 J. Ruiz, A. J. Mota, A. Rodríguez-Diéguez, S. Titos, J. M. Herrera, E. Ruiz, E. Cremades, J. P. Costes and E. Colacio, *Chem. Commun.*, 2012, **48**, 7916–7918.
31 I. Oyarzabal, J. Ruiz, J. M. Seco, M. Evangelisti, A. Camón, E. Ruiz, D. Aravena and E. Colacio, *Chem. – Eur. J.*, 2014, **20**, 14262–14269.
32 J. P. Costes, S. Titos-Padilla, I. Oyarzabal, T. Gupta, C. Duhayon, G. Rajaraman and E. Colacio, *Inorg. Chem.*, 2016, **55**, 4428–4440.
33 T. Gupta, M. F. Beg and G. Rajaraman, *Inorg. Chem.*, 2016, **55**, 11201–11215.
34 J. A. Mydosh, *Spin Glasses*, Taylor & Francis, Washington, DC, 1993.
35 S. Tripathi, A. Dey, M. Shanmugam, R. S. Narayanan and V. Chandrasekhar, *Top. Organomet. Chem.*, 2019, **64**, 35–75.
36 J. Juráková, J. Dubnická Midlíková, J. Hrubý, A. Kliuikov, V. T. Santana, J. Pavlik, J. Moncoľ, E. Čižmár, M. Orlita, I. Mohelský, P. Neugebauer, D. Gentili, M. Cavallini and I. Šalitroš, *Inorg. Chem. Front.*, 2022, **9**, 1179–1194.
37 D. Gatteschi and R. Sessoli, *Angew. Chem., Int. Ed.*, 2003, **42**, 268–297.
38 K. Saito and S. Miyashita, *J. Phys. Soc. Jpn.*, 2001, **70**, 3385–3390.
39 S. Gómez-Coca, D. Aravena, R. Morales and E. Ruiz, *Coord. Chem. Rev.*, 2015, **289–290**, 379–392.
40 Y. Peng, M. K. Singh, V. Mereacre, C. E. Anson, G. Rajaraman and A. K. Powell, *Chem. Sci.*, 2019, **10**, 5528–5538.
41 Y. H. Zhou and J. Lin, in *Journal of Alloys and Compounds*, Elsevier, 2006, vol. 408–412, pp. 856–859.
42 J. Cepeda, S. Pérez-Yáñez, G. Beobide, O. Castillo, J. Á. García and A. Luque, *Eur. J. Inorg. Chem.*, 2015, **2015**, 4318–4328.
43 X. L. Li, J. Li, C. Zhu, B. Han, Y. Liu, Z. Yin, F. Li and C. M. Liu, *New J. Chem.*, 2018, **42**, 16992–16998.